RESEARCH PAPER

Field Displacement-Based Inverse Method for Elastic and Viscoelastic Constitutive Properties

G. Nsengiyumva[1] · Y-R. Kim[1]

Abstract

Background Mechanical characterization of materials that solely relies on global responses may overlook important local behavior that significantly affects the characterization of material properties. Field displacements such as from digital image correlation (DIC) can provide high-fidelity experimental data, which combined with finite element method (FEM) can form DIC-FEM inverse method that can better account for complex mechanical properties of materials. Despite its capability, the DIC-FEM inverse method has been mainly applied to an elastic-dominant regime even though inelastic deformation is important in many engineering materials. Specifically, the DIC-FEM inverse method has not been fully extended to viscoelastic materials due to the complex representation of the time-dependent modulus.

Objective This study aimed at establishing a DIC-FEM inverse framework to identify constitutive properties of homogeneous elastic and viscoelastic materials.

Methods Two example materials (i.e., polyetheretherketone (PEEK) and a viscoelastic fine aggregate matrix (FAM) with a bituminous binder) were selected for the elastic and viscoelastic investigation, respectively. Both were experimentally tested using three-point bending incorporated with DIC. FEM simulated the experiment and the Nelder-Mead nonlinear optimization algorithm was implemented to solve the inverse problem.

Results The DIC-FEM inverse method successfully identified Young's modulus of an example linear elastic PEEK and the linear viscoelastic relaxation modulus of FAM.

Conclusions The resulting DIC-FEM inverse method is applicable to various materials with inelastic deformation and can be extended to localized behavior induced by microstructure heterogeneity and fracture.

Keywords Field displacements · Digital image correlation · DIC-FEM inverse method · Viscoelasticity

Introduction

Mechanical characterization of materials that solely takes global responses may overlook important local behavior (localized deformation), particularly behavior that significantly affects material properties. Although global responses are sufficient for identifying mechanical properties in simple boundary value problems (BVPs), they can produce misleading mechanical properties in more complicated BVPs that include heterogeneity, anisotropy, and highly localized phenomena, such as fracture. Soft materials are a prime example where using global results can result in inaccurate properties. This is mainly due to higher deformations near loading areas relative to the rest of the specimen. Locally-measured responses are important to more accurately characterize the materials [1].

Local results, such as field displacements measured during the experiments, can be obtained using a digital image correlation (DIC) technique [2–5]. The local results provide higher fidelity information that is useful in accurately characterizing the thermo-mechanical behavior of materials [6–9]. DIC was pioneered by Sutton et al. [10, 11]. DIC takes displacements from successive images during the time that a specimen undergoes deformation. The perceived pixel movement between images is correlated to equivalent deformation gradients. DIC has been used in diverse fields, including rigid

✉ Y-R. Kim
yong-rak.kim@tamu.edu

G. Nsengiyumva
gabriel.nsengiyumva@tamu.edu

1 Zachry Department of Civil and Environmental Engineering, Texas A&M University, College Station, TX 77843-3136, USA

body motions, experimental mechanics for displacement measurements, and deformation characterization of various nonlinear material behavior. For example, full-field kinematic measurements from DIC have been used to:

- identify material properties and validate constitution in soft materials (such as rubber) and heterogenous biological tissues where traditional methods—such as strain gauges—are impractical [9, 12].
- experimentally investigate thin films and characterize their behavior within a small elastic regime that is otherwise difficult to gauge [13–15].
- detect three-dimensional (3D) out-of-plane behavior for circular cylindrical specimens under compression and identify the barreling profile [16].
- evaluate kinematics and characterize constitutive properties of fiber-reinforced composite materials and laminates [17–19].

Additionally, the field displacement measurements from DIC can be integrated with computational model simulations such as the finite element method (FEM) to inversely characterize material properties [20–22]; this is done by penalizing the objective error function between experimental results and computational simulation results [21, 23–25]. The DIC-FEM method can be classified as the FEMU (finite element method update) [26]. Other local-based inverse methods include the I-DIC (integrated DIC) [27] and VFM (virtual fields method) [28–30]. The I-DIC used an analytical solution to formulate the objective function after DIC results, while the VFM is based on the virtual fields method objective function.

The DIC-FEM method can better account for material heterogeneity, anisotropy, nonlinear inelasticity, and damage by effectively accommodating complicated geometries and mechanical properties [12, 31, 32]. The DIC-FEM inverse method has been mainly applied to an elastic-dominant regime [6, 9, 12, 13, 33–39] and some materials presenting elastoplastic or plastic deformation [40–42]. The DIC-FEM method has not been fully extended to viscoelastic materials yet due to the complex representation of the time-dependent modulus [43, 44]. This study proposes a DIC-FEM inverse method with the ability to extend characterizing the properties of viscoelastic materials. The specific objectives of this study are:

- To establish a DIC-FEM inverse framework to identify constitutive properties of homogenous elastic and viscoelastic materials.
- To validate the resulting DIC-FEM inverse framework by employing two example materials: an elastic poly-

etheretherketone (PEEK) and a viscoelastic fine aggregate matrix (FAM) with a bituminous binder.

Research Methodology

To meet the objectives, the methodology shown in Fig. 1 was adopted. The research method is composed of three parts: inputs (selected materials), DIC-FEM framework, and output (target material properties). Two example materials were selected for the elastic and viscoelastic investigation. Subsequently, laboratory testing specimens of each material were incorporated with DIC to measure field displacements followed by FEM to simulate the testing. ABAQUS [45], a commercial finite element analysis (FEA) package, was used to model the testing setup (i.e., specimen geometry, loading, and boundary conditions) with the corresponding constitutive behavior (e.g., elastic and viscoelastic). The DIC-FEM inverse method iteratively modified material properties within FEA to minimize the difference between DIC and FEM displacement results.

FEA was conducted via a Python script that was developed to adaptively control ABAQUS FEA material inputs, wait for FEA job completion, and extract kinematic results at the specified location (i.e., region of interest (ROI) nodes). In parallel, DIC measurement results were obtained from the experimental testing using VIC-3D, a commercial DIC software, to correspond with spatial coordinates of ROI nodes from FEA. Subsequently, MAT-LAB was used for optimization via the built-in function of *fminsearch()* that implements the Nelder-Mead (N-M) solver. Kowalewski and Gajewski [46] showed that N-M algorithm is quickly converged when used with DIC and FEM data. For each iteration, a batch script was used to trigger the Python code, which then performed FEA. The iterations continued until a convergence of the objective function was achieved.

The objective function for the inverse method was formulated around the spatially matched displacement results within a ROI, as shown in Fig. 2. It is noteworthy that the ROI was selected in the region of the specimen where higher deformation magnitude was expected.

DIC displacement data were analyzed in MATLAB to facilitate reducing the inherent noise associated with DIC data [47]. For example, a combination of MATLAB built-in functions such as *interp()*, *dfilt()*, and *smooth()* were used to interpolate data, filter and smoothen DIC data to prepare for the DIC-FEM inverse method, as exemplified in Fig. 3.

Fig. 1 Framework for the DIC-FEM inverse method implemented in this study
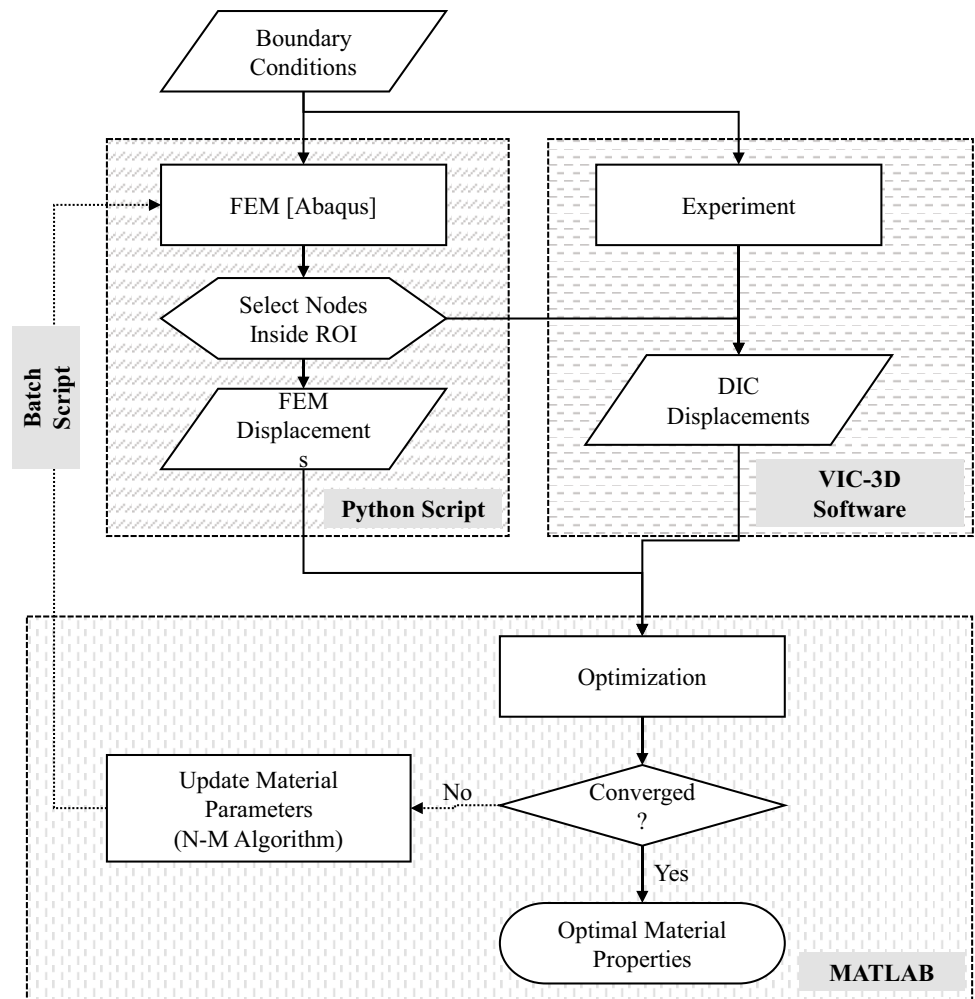
DIC Method

DIC takes successive images during the time that a specimen undergoes loading and deducing of field displacements and subsequently calculated deformation by correlating (i.e., back-calculate) deformation gradients of several sections of the image (i.e., subsets) [10, 47, 48]. The success of DIC is thus highly dependent on ensuring the uniqueness of the subsets to allow convergence of the correlation function. The uniqueness of subsets was achieved by applying random, contrasting, isotropic, and non-repetitive speckles on the surface of the specimen.

In this study, a subset DIC was used in which a subset of pixels is subjected to a two-dimensional deformation Fig. 4(a). Points (x, y) in the reference image correspond to $(\widetilde{x}, \widetilde{y})$ points in the deformed image. The mapping function between the two points is [10, 47]:

$$
\begin{aligned}
\widetilde{x} &= x + u \\
\widetilde{y} &= y + v
\end{aligned}
\tag{1}
$$

where u and v are the displacement components that can be approximated at different orders using the Taylor series expansion method. The second-order expansion around a point (x_0, y_0) leads to the following mapping functions [10, 47]:

$$
\begin{aligned}
\widetilde{x} &= x_o + u_o + u_x\Delta x + u_y\Delta y + \tfrac{1}{2}u_{xx}\Delta x^2 + \tfrac{1}{2}u_{yy}\Delta y^2 + u_{xy}\Delta x\Delta y \\
\widetilde{y} &= y_o + v_o + v_y\Delta y + v_x\Delta x + \tfrac{1}{2}v_{yy}\Delta y^2 + \tfrac{1}{2}v_{xx}\Delta x^2 + v_{xy}\Delta x\Delta y
\end{aligned}
\tag{2}
$$

where $\Delta x = (x - x_o)$ and $\Delta y = (y - y_o)$. There are twelve parameters of the mapping function presented in Eq. (2): u_0 and v_0 are displacement components at (x_o, y_o); u_x, v_x, u_y, v_y are the components of the first-order gradient; and u_{xx},

Fig. 2 DIC and FEM of an example beam specimen with a region of interest (ROI): (**a**) DIC with a ROI; and (**b**) finite element model with a ROI
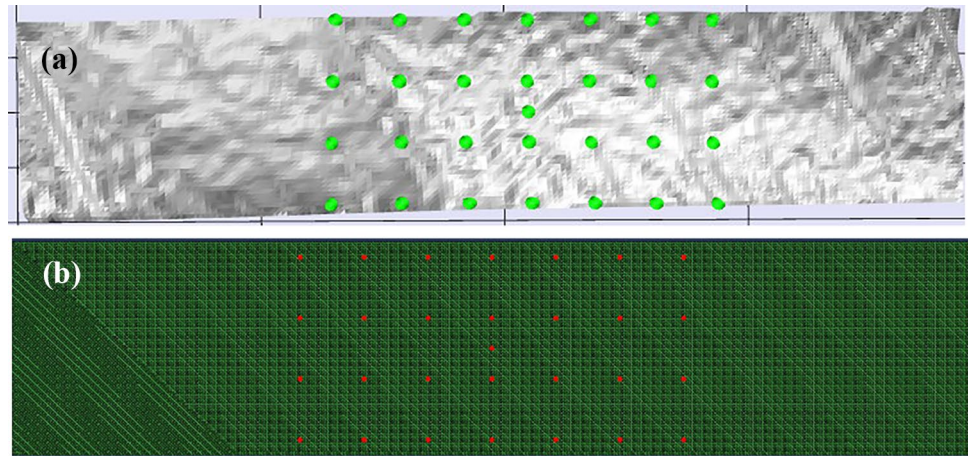
v_{xx}, u_{yy}, v_{yy}, u_{xy}, v_{xy} are the components of the second-order gradient.

A higher order of approximation yields a more accurate representation of the deformation in the subset. Despite being a contactless technique, DIC yields highly accurate results that can achieve sub-micron (sub-pixel) resolution [49]. During image acquisition, there is a possibility of light intensity change that can offset the gray-scale values of images. To account for the offset, an additional parameter ω is introduced for offset in the gray-scale value between consecutive images. Therefore, the correlation calculates a vector $P = \{u_o, v_o, u_x, v_x, u_y, v_y, u_{xx}, v_{xx}, u_{yy}, v_{yy}, u_{xy}, v_{xy}, \omega\}$ that represents the 13 parameters (i.e., 12 from Eq. (2) and ω) in the mapping function. A least-square correlation coefficient is used in the calculation [47].

As the subsets selected are discrete groups of pixels, it is possible to have undesired discontinuities at the subset boundaries, as illustrated in Fig. 4(a). To mitigate this issue, a step between adjacent subsets was used to ensure

the overlap and displacement compatibility [see Fig. 4(b)]. The subset DIC method has been used in this study to obtain measurement resolutions of 4.8 nm for in-plane measurements [49]. Another study by Lu and Cary [50] obtained an accuracy of $\pm 10^{-4}$ per pixel.

DIC-FEM Optimization Method

The objective function for optimization was calculated as the root of the summed squares of the differences between FEM and DIC displacements. The Nelder-Mead (N-M) solver [51] was adopted for the optimization over other conventional solvers—such as the Newton–Raphson solver—due to its robustness, derivative-free nature, and ease in incorporating constrain functions as part of the objective function [51].

The N-M algorithm uses a simplex to construct vertexes (e.g., material properties) around the initial guess; this is followed by a replacement of the vertex with the

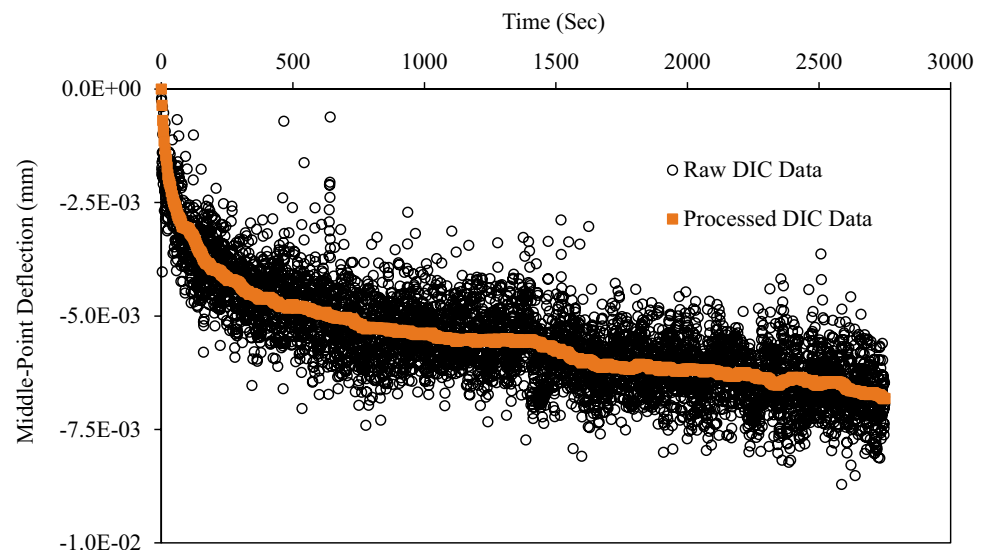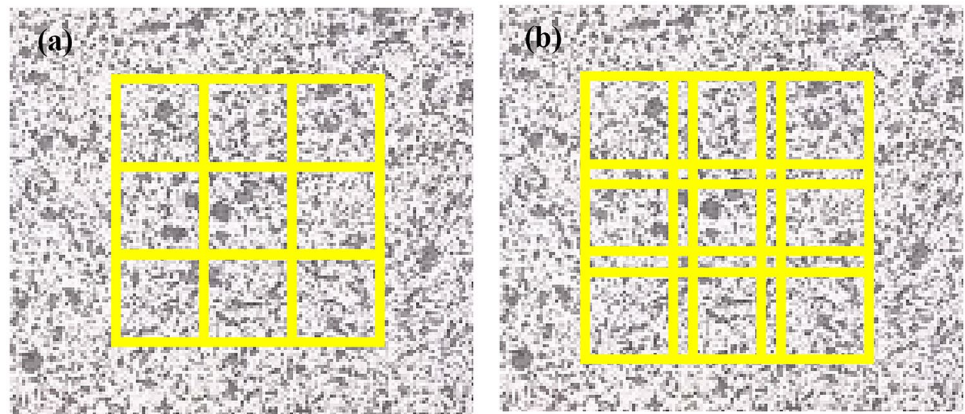**Fig. 3** Example of DIC data processing in MATLAB

highest function value through a series of reflections, contractions, and expansions [38, 52, 53]. For example, given a vector χ to optimize (e.g., [1.0, 1.0]), N-M composes an initial simplex with vertices: χ_1, $\chi_2 = \chi_1 + (\alpha, 0)^T$ and $\chi_3 = \chi_1 + (0, \alpha)^T$, where the coefficient α controls the step size of the algorithm (Fig. 5). Subsequently, the vertex with the highest function value (e.g., χ_1) undergoes a replacement process. An iteration is completed once a vertex has been replaced. The optimization continues until a stopping criterion—such as a decrease between two iterations, the maximum number of iterations, or a sufficiently small function value $\Psi_u(\chi)$ [54] —is met. The N-M solver has been successfully used to identify constitutive properties in elastic materials [34, 37].

Since the N-M solver is a constraint-free method, the constraints were externally imposed by the penalty method [25] in this study; a large number was assigned to the function value if the χ was outside the boundary domain Ω_χ [55]. An example of a reasonable constraint is that the elastic modulus is always positive (i.e., $E \geq 0$). The final objective function is shown as follows:

$$\min_{\chi \in \mathbb{R}^N} \Psi_u(\chi) = \begin{cases} \|u_{DIC} - u_{FEM}(\chi)\|_2 & \text{if } \chi \in \Omega_\chi \\ 10^{20} & \text{for } \chi \notin \Omega_\chi \end{cases} \quad (3)$$

where $\Psi_u(\chi)$ is the objective function, χ is a vector of size N material properties, u_{DIC} is experimental displacements from DIC, $u_{FEM}(\chi)$ is the computational displacements from FEM at χ, and $\| \cdot \|_2$ is the Euclidian norm.

Experimental Test Set-Up

Figure 6 shows the experimental testing setup used in this study. It is comprised of a mechanical testing station and a DIC system. The hardware for DIC included a high-capacity desktop computer to store images Fig. 6(a), two stereo cameras Fig. 6(b), two light sources Fig. 6(c), and a data acquisition system (DAQ). The mechanical testing station included a desktop computer, a load-frame, a loadcell of 3kN capacity, a testing fixture, and a DAQ. Since the mechanical testing station and the DIC were two completely different systems, they were synchronized through their respective
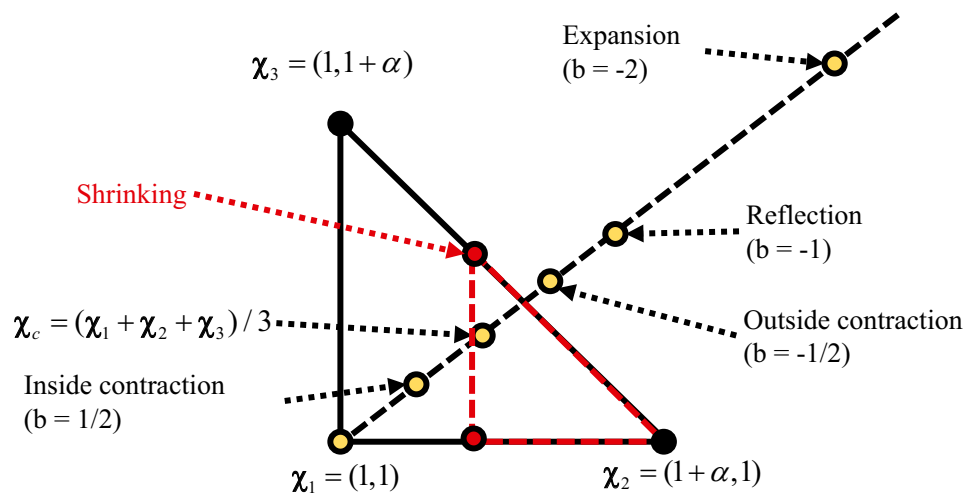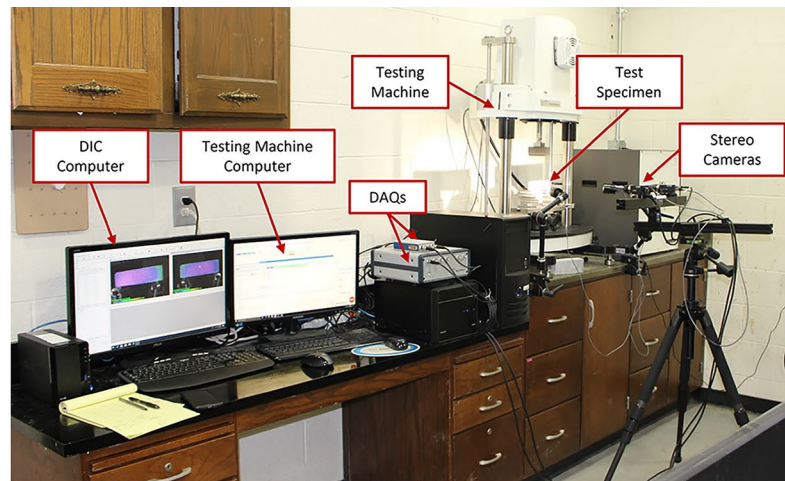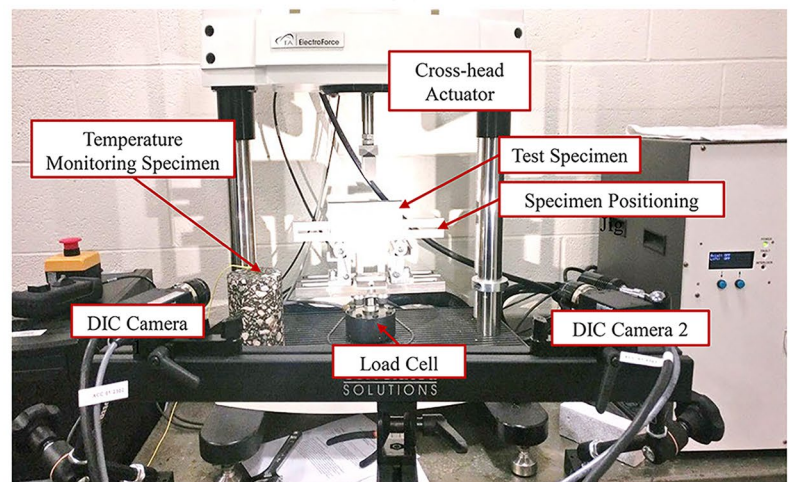
Fig. 5 Nelder-Mead Simplex Algorithm for χ
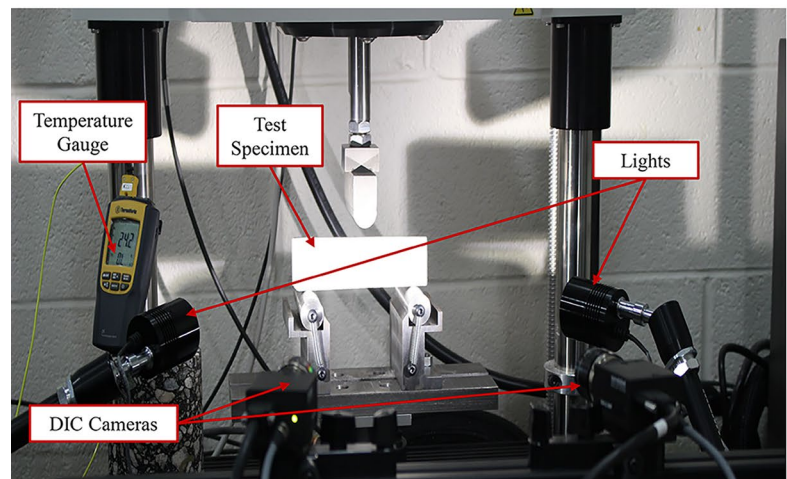
Fig. 6 Experimental set-up: (**a**) the entire set-up showing DIC and mechanical testing station (3kN capacity); (**b**) detailed close-up view of the testing set-up; and (**c**) set-up with light source

(a)

(b)

(c)

DAQs via BNC cables for load and trigger information communication. As a result, the DIC image acquisition could be controlled to commence at the same time as the mechanical test is conducted. Linking both systems was important, as each DIC image could be coupled with a known loading stage for subsequent data analyses.

The DIC analysis software used in this study was Vic-3D v7.0, which used another software called Vic-Snap LS for image acquisition during testing. For the DIC processing, a computer with quad-core 3.5 GHz Intel i7 CPU, 500 GB solid-state and 4 TB disk storage, 32 GB RAM, and Windows 10 operating system. The cameras for image acquisition were two digital cameras of 2.3 Megapixels with a resolution of 1920×1200 pixels at a 162 frame rate. The camera had a one-inch sensor and was paired with two Schneider Cinegon lenses with a 1.8/16 mm aperture/focal length. The lighting system was composed of two white LEDs that illuminated the test specimen that was sprayed with a speckle pattern. It is noteworthy that before DIC measurement, images of a composite grid at several random camera-facing angles (e.g., 25) were taken for calibration.

Materials and Sample Fabrication

Polyetheretherketone (PEEK)

PEEK is a thermoplastic semi-crystalline polymer [56]. It was selected as the example material for the elastic investigation. PEEK has a high strength-to-weight ratio and is resistant to wear, and it also presents excellent biocompatibility [57]. In this study, PEEK was considered as a homogenous time-independent elastic material with the general constitutive relationship between stress and strain expressed as follows:

$$\sigma_{ij} = \frac{Ev}{(1+v)(1-2v)}\delta_{ij}\varepsilon_{kk} + \frac{E}{1+v}\varepsilon_{ij} \qquad (4)$$

where σ_{ij} is the stress tensor; v = Poisson's ratio; ε_{ij} is the strain tensor; E is the elastic (Young's) modulus. Note that E and v are the only two independent constants to establish the stress–strain relationship in the case of PEEK.
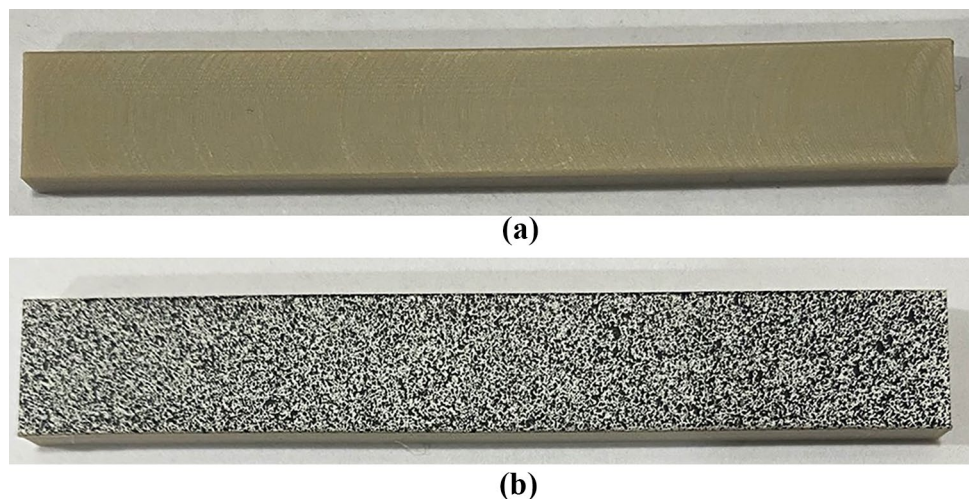
PEEK sample material was commercially acquired from Macmaster Carr, and the specimens were machined to geometry specifications of 75 mm, 10 mm, and 4 mm for length, height, and thickness, respectively. Before testing with the DIC, speckle patterns were applied on the specimen's surface by spraying a white base paint; after the white layer dried, a speckle of black (sprayed) dots were added. Figure 7 shows the PEEK specimen before Fig. 7(a) and after Fig. 7(b) application of the speckles. Several spraying techniques were attempted to select the optimal speckle preparation method. The condition of the speckle was that it should be isotropic, random, statistically homogenous, non-repetitive, and have high contrast. All the conditions were properly met by spraying black dots on a painted white surface. It should be noted that the sizes of the black dots were adjusted depending on the size of the specimens in order to maintain a high-contrast speckle pattern.

A three-point bending test was performed on the specimen with a span length of 60 mm. The geometry of the PEEK specimen satisfies the requirement of ASTM D790. The testing was conducted at 23 °C in a displacement-controlled mode with a monotonic loading of 10 mm/min. The test terminated with a load of 350 N. It is worth noting that the yield stress for the PEEK is around 120 MPa [56, 58, 59]. PEEK remained within the linear elastic region throughout the testing in this study. The test setup for PEEK is shown in Fig. 8.

Fine Aggregate Matrix (FAM) with Bitumen

FAM is the primary component of typical asphalt concrete (AC) mixtures [60]. It was selected in this study as an example of viscoelastic material. FAM is considered to be the matrix phase within AC mixtures, and it is composed of fine aggregates passing through a No. 16 sieve (mesh size of 1.2 mm) and a bituminous binder [61]. Many studies—including Im et al. [62], Aragao et al. [63], Kim et al. [64], and Ban et al.
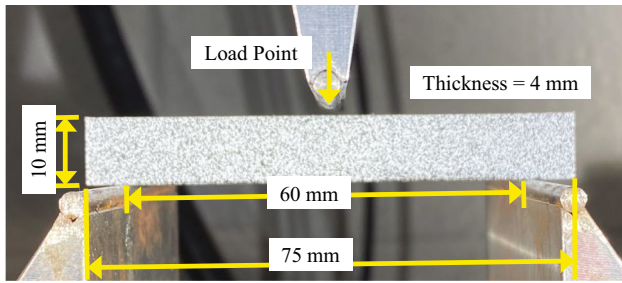
Fig. 7 Example of DIC sample preparation of PEEK: (**a**) before applying speckles; and (**b**) after applying speckles

(a)

(b)

Fig. 8 Three-point bending test set-up for PEEK specimen

[65] —presented time- and rate-dependent viscoelastic behavior of the FAM at different loading conditions. FAM is considered to be isotropic as the ratio of the specimen geometry to maximum particle size is high (i.e., about 30), and particles are randomly distributed within the FAM microstructure.

In this study, FAM was considered as an isotropic, homogenous viscoelastic material with the general constitutive relationship between stress and strain expressed as follows:

$$\sigma_{ij} = \frac{v}{(1+v)(1-2v)} \int_0^t E(t-\tau)\delta_{ij}\frac{\partial \varepsilon_{kk}}{\partial \tau}d\tau + \frac{1}{1+v}\int_0^t E(t-\tau)\frac{\partial \varepsilon_{ij}}{\partial \tau}d\tau \tag{5}$$

where σ_{ij} is the stress tensor; v = Poisson's ratio; $E(t)$ = viscoelastic stress relaxation modulus; ε_{ij} is the strain tensor; δ_{ij} = Kronecker delta; and τ = integration variable.

The isotropic uniaxial relaxation modulus, $E(t)$, in an isothermal condition can be expressed in the Prony series representation as follows [66]:

$$E(t) = E_\infty + \sum_{i=1}^m E_i e^{\frac{-t}{\rho_i}} \tag{6}$$

where E_∞ and E_i are the spring constants in the generalized Maxwell model, ρ_i is the relaxation time, and m is the number of Maxwell units in the generalized Maxwell model. Similarly, the linear viscoelastic creep compliance can also be expressed in Prony series as [66]:

$$D(t) = D_g + \sum_{j=1}^n D_j \left(1 - e^{\frac{-t}{\tau_j}}\right) \tag{7}$$

where D_g and D_j are the glassy compliance and retardation strength, respectively in the generalized Kelvin model, τ_j is the retardation time, and n is the number of Voigt units in the generalized Kelvin model. The $E(t)$ and $D(t)$ expressed in the Prony series are interconvertible, as shown by Park and Schapery [66].

To prepare FAM specimens, fine aggregates were mixed with an eight weight percent of the bituminous binder at the mixing temperature of 160 °C [60]. The mixed loose

FAM materials were then compacted at 149 °C (compaction temperature) to produce a cylindrical sample of 170 mm in height and 150 mm in diameter using a Superpave gyratory compactor. Before the compaction, the loose FAM mixture was cured for two hours at 135 °C to induce short-term aging [67]. Beam FAM specimens were then prepared from the cylindrical sample by cutting, as shown in Fig. 9(a). In total, one cylinder-compacted sample produced 10 beam specimens (150 mm in length, 35 mm in height, and 25 mm in thickness). The specimens were then subjected to flexural beam creep testing, as shown in Fig. 9(b).

To find the load limit of linear viscoelastic behavior of the FAM mixture specimen, a preliminary investigation was conducted on the FAM beam specimen by applying different levels of constant creep loads (for creep testing). Within the linear viscoelastic condition, the beam deflection is directly and linearly proportional to the applied creep load, as the material satisfies linear viscoelastic conditions [68]. Thus, creep tests were conducted at increasing load levels until the linearity condition was violated. In this study, the linear viscoelastic limit was examined based on the homogeneity concept (i.e., linear scaling), where the creep compliance $D(t)$ remains identical within the linear viscoelastic range. To calculate the time-varying viscoelastic creep compliance $D(t)$ at each loading level, an analytical solution that relates the beam deflection to linear viscoelastic properties was used. In an attempt to obtain the analytical solution, the elastic solution for the Timoshenko beam theory [69] was converted into a viscoelastic solution using the elastic–viscoelastic correspondence principle [70]. The resulting time-varying deflection as a function of the creep compliance is as follows:

$$u^T(t) = \left(\frac{P_o L^3}{48I} + \frac{2M_o(1+v)}{AKs}\right)D(t) \tag{8}$$

where $u^T(t)$, P_o, and M_o are the deflection at the middle center of the beam, creep load, and bending moment, respectively. A, L, I, and K_s are cross-sectional area, span length between two supports, the second moment of inertia, and the Timoshenko shear coefficient [71], respectively. It should be noted that Poisson's ratio is assumed to be time-independent. The bending moment of the simply-supported beam can be obtained as $M_o = P_o L/4$, which results in the following deflection equation:
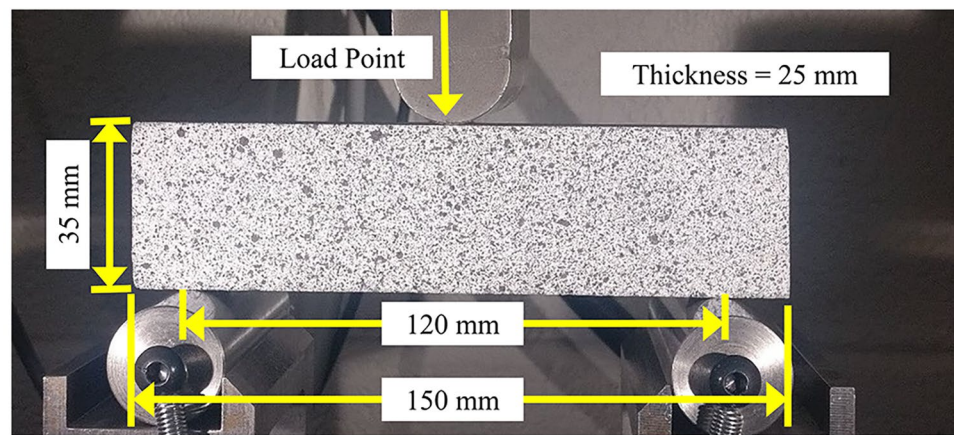
$$\begin{aligned} u^T(t) &= P_o B(t) \\ B(t) &= \left(\frac{L^3}{48I} + \frac{2L(1+v)}{4AKs}\right)D(t) \end{aligned} \tag{9}$$

As previously mentioned and shown in Eq. (9), the middle-center deflection $u^T(t)$ is directly and linearly proportional to the applied creep load P_o. It is noteworthy that the middle center deflection was easily obtained from DIC.

Fig. 9 FAM testing: (**a**) sample fabrication; (**b**) three-point bending beam test set-up
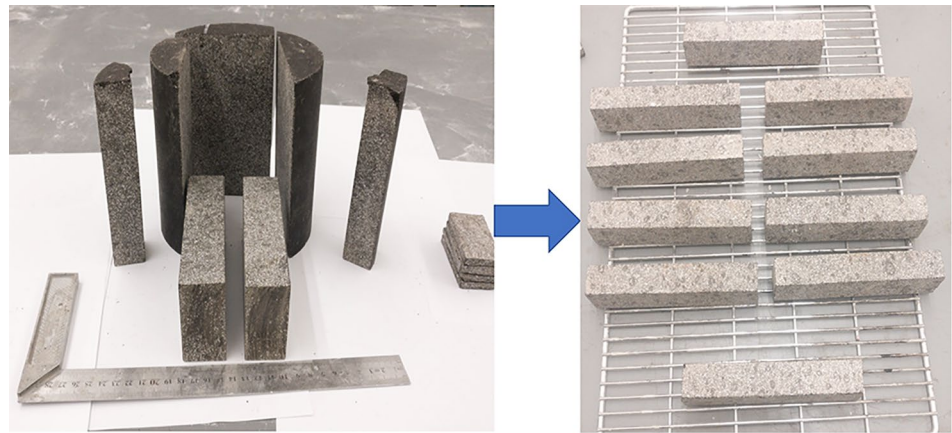
(a)

(b)

Figure 10 shows the creep compliance $D(t)$ calculated from three varying creep loads of 2.5 N, 5 N, and 10 N; all other testing conditions remained identical during testing. It appears that the creep compliance was similar between the two smaller loads of 2.5 N and 5.0 N. Changes were noticed beyond 5.0 N, implying an onset of nonlinear viscoelastic
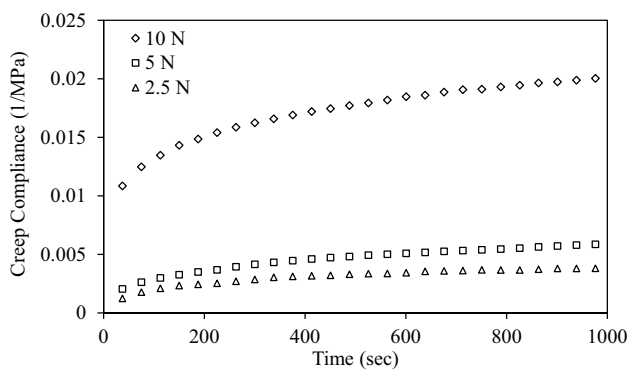

Fig. 10 FAM creep compliance from three varying creep loads of 2.5 N, 5 N, and 10 N

response. Since an appropriate creep load for the subsequent DIC-FEM inverse method should be within the linear viscoelastic limit, a sufficiently small creep load that does not cause nonlinear viscoelastic deformation is necessary. Based on the observation in Fig. 10, a load of 2.5 N was selected for the subsequent DIC-FEM inverse method in order to ensure linear viscoelastic conditions during FAM testing. It should be noted that the creep testing shown in Fig. 10 was conducted on a representative FAM specimen loaded for 1,000 s of creep loading and unloaded for 24 h to ensure a full recovery of creep deformation. During the unloading period, the specimens were removed from the testing fixture to avoid any additional flexural creep resulting from gravity. The loading–unloading test sequence of each specimen was taken from the smallest load (2.5 N) to the larger loads with a careful control of positioning of the specimen, so that each creep testing can be conducted at the same boundary conditions. Furthermore, the testing temperature was carefully controlled and monitored using an embedded thermocouple with a dummy sample.

Fig. 11 Horizontal strain (ε_{xx}) profile of (**a**) DIC; and (**b**) FE results
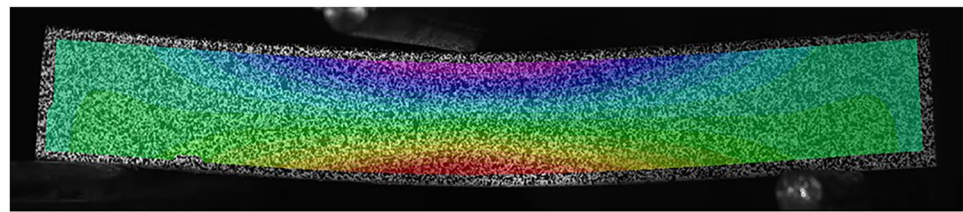
(a) DIC image of PEEK beam under three-point bending
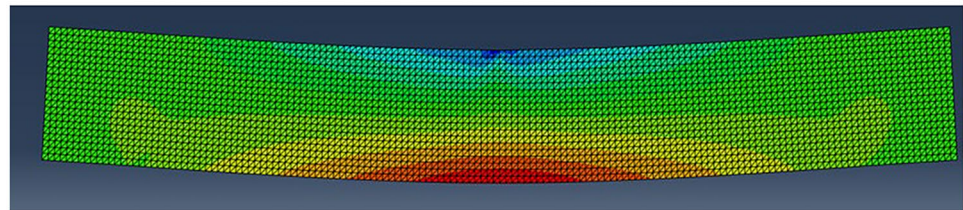
(b) FE model simulation results of PEEK beam under three-point bending

Results and Discussion

Elastic Modulus of PEEK

DIC data were analyzed using a subset size of 25×25 pixels and a step size of 8 pixels Fig. 11(a). Concurrently, the FE simulation was conducted using a 0.5 mm mesh of 3-node linear elements (CPS3) Fig. 11(b). The FEM boundary conditions were applied via prescribed nodal displacement. The plane stress assumption was made as the FEM simulation results are compared to 2-D DIC image data, and it was helpful to reduce computational costs as the DIC-FEM process requires a large number of iterative computation. The mesh size was selected after a mesh convergence study. Equation (3) was then used to construct the objective function from DIC and FEM displacement results inside the ROI. For the PEEK elastic properties, a total of 697 points were used to calculate the objective function at each iteration.

As shown in Eq. (4), there are two independent elastic properties (i.e., E and v) for PEEK when one considers a homogenous time-independent elastic material. Poisson's ratio was assumed reasonably with a constant of 0.35 [72]. This simplification is valid as the three-point beam testing that does not consider three-dimensional deformation in particular with the anticlastic curvature is not feasible to characterize Poisson' ratio. In this study, both the DIC measurements and FEM model simulations were conducted in two-dimensional space. Therefore, the sole identification of Young's modulus of the PEEK from the DIC-FEM inverse process is necessary.

The results of the DIC-FEM inverse method to calculate Young's modulus (E) are shown in Fig. 12(a), where the optimal E value was 3,951.8 MPa. The resulting modulus value was in good agreement with the typical values found in the PEEK-related literature [59, 73–75]. Figure 12(a) also shows the evolution of the objective function during the optimization process. As shown, the solution converged reasonably at approximately 20 iterations. Figure 12(b) presents the resulting displacements at the optimized elastic modulus. Five different locations were arbitrarily selected to demonstrate the agreement between DIC experimental results and FEM computational simulations. Generally, the displacements were in good agreement at the optimal E value found, implying the validity of the DIC-FEM inverse process in identifying unknown material properties, such as Young's modulus in this example.

Viscoelastic Relaxation Modulus of FAM

The creep testing was conducted using the predetermined creep load (i.e., 2.5 N) with a total creep time of 2,750 s. DIC data was analyzed using a subset size of 25×25 pixels and a step size of 8 pixels. The FE model simulation was conducted using a 0.5 mm mesh of 3-node linear elements (CPS3), which was determined through a mesh convergence study. The FEM modeling boundary conditions were applied via prescribed nodal force, and plane stress condition was assumed.

Similar to the elastic PEEK case, there are two independent viscoelastic properties (i.e., $E(t)$ and v) for FAM when one considers a homogenous time-dependent linear viscoelastic material. Tschoegl et al. [76] noted the difficulty in experimentally measuring Poisson's ratio in viscoelastic materials, and Lu et al. [77] recommended 4-figure precision for accurate identification of Poisson's ratio. The DIC used in the present study is limited to providing the level of accuracy necessary due to the noise level (Fig. 3) from displacements. The noise from displacements would propagate to strain calculations as well. This limitation can be overcome with more accurate DIC technologies such as
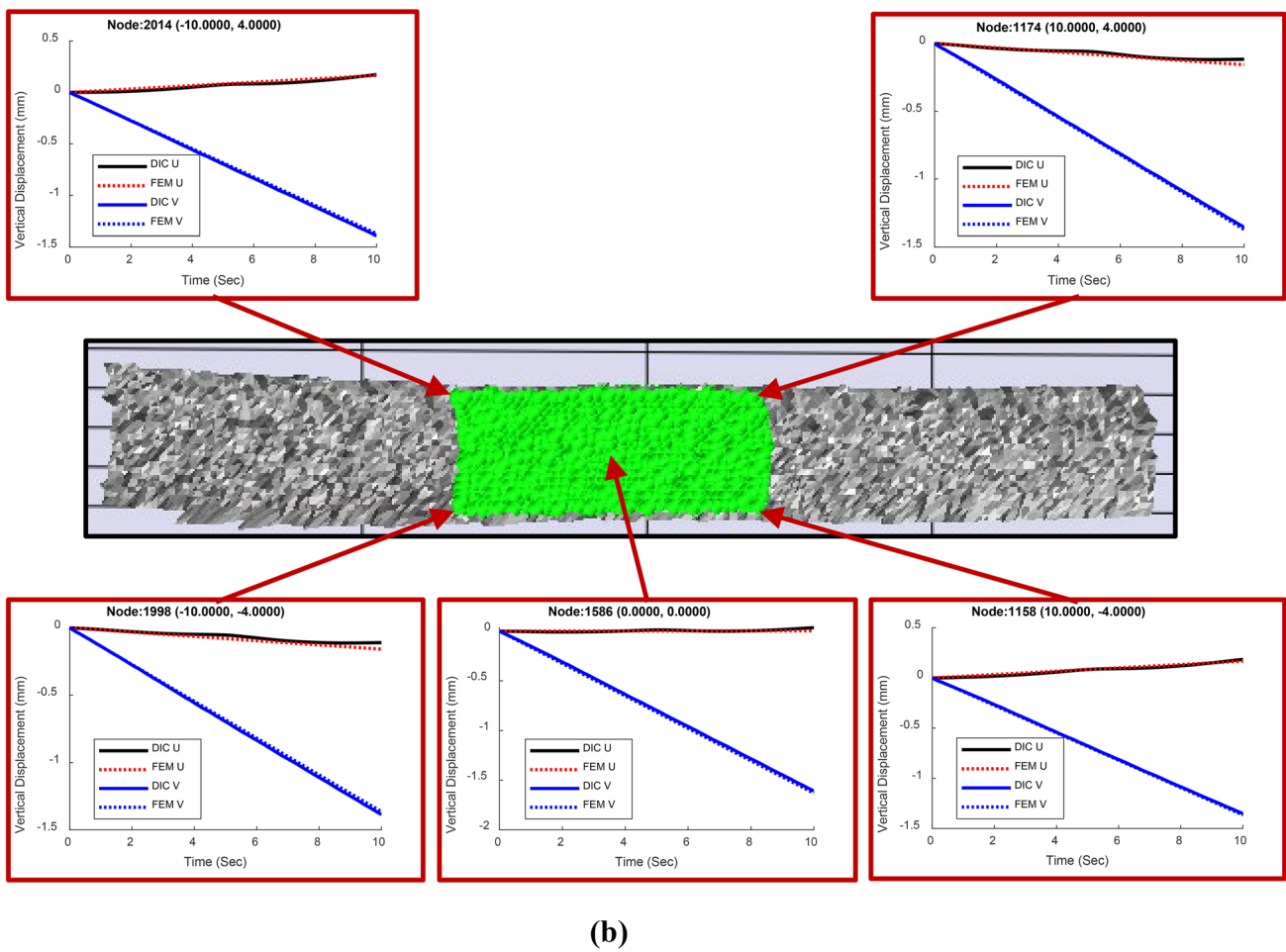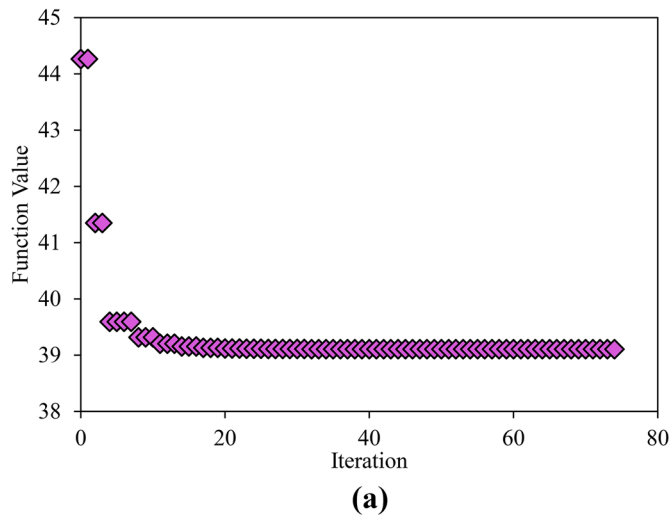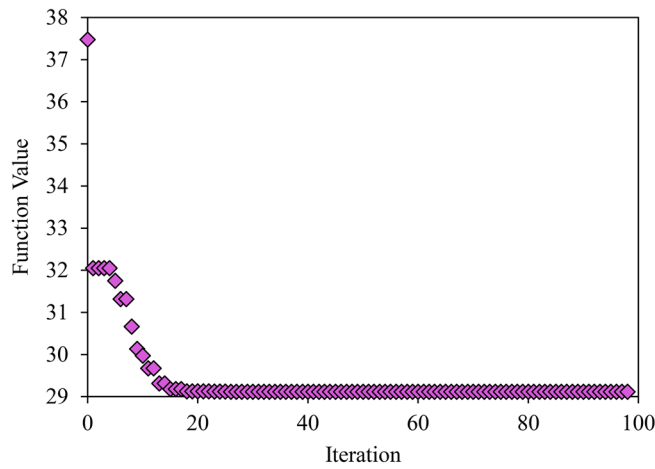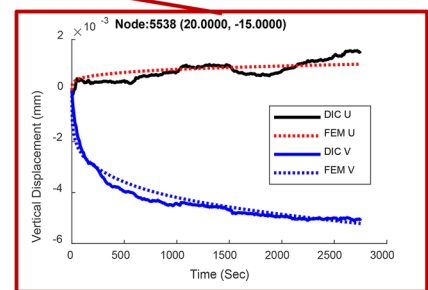
(a)

(b)

Fig. 12 Results from the DIC-FEM inverse method for PEEK: (**a**) evolution of objective function; and (**b**) comparison of displacements at the solution

(a)
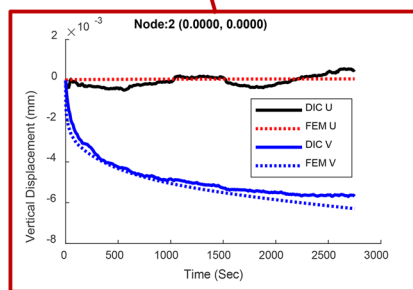
(b)

Fig. 13 Results from the DIC-FEM inverse method for FAM: (**a**) evolution of objective function; and (**b**) comparison of displacements at the solution

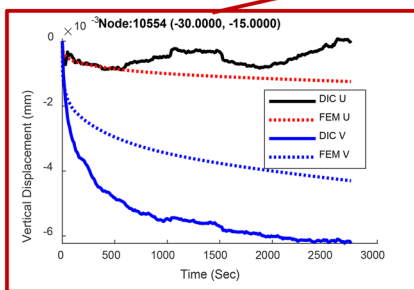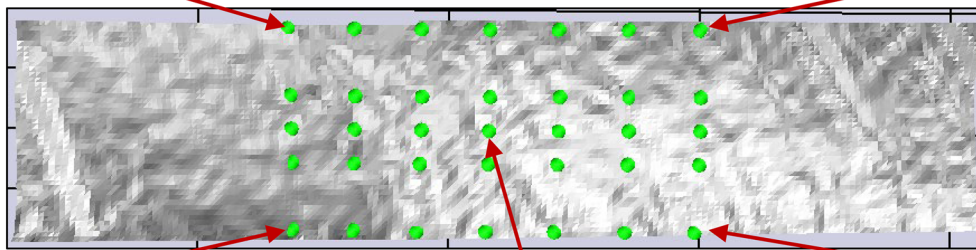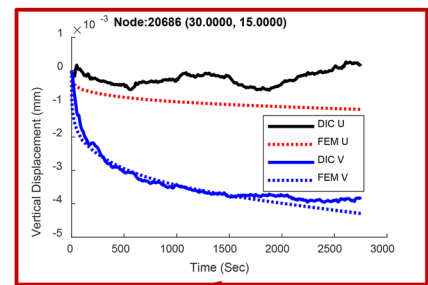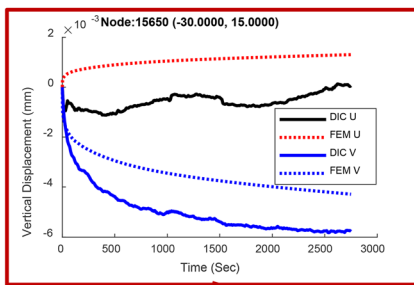| Prony Series Parameters	
ρ_i (sec)	E_i (MPa)
1.00E-05	9.25E+03
1.13E-04	3.28E+03
1.29E-03	2.72E+03
1.46E-02	1.51E+03
1.66E-01	1.15E+03
1.88E+00	5.51E+02
2.14E+01	3.42E+02
2.42E+02	1.83E+02
2.75E+03	1.44E+02
E_∞	4.18E+02

**Table 1** Resulting Prony Series Parameters from the DIC-FEM Inverse Method

$$E(t) = E_p + E_q t^{-r} \tag{10}$$

where $E(t)$ is relaxation modulus, E_p is long-time equilibrium modulus, E_q is a regression constant, and r is a regression constant representing the slope between modulus and time.

The generalized power law is in a form of the combination of the instantaneous and transient parts. Next, the generalized power law parameters calibrated at each iteration automatically generate time-dependent relaxation modulus data which were then converted to the generalized Maxwell model represented by the Prony series [Eq. (6)]. This is because the FEM model simulation requires the viscoelastic relaxation modulus in the form of the generalized Maxwell model. The Prony series parameters are composed of ten spring constants (E_∞, and E_1 to E_9) and nine relaxation times (ρ_1 to ρ_9) which can effectively cover nine decades of relaxation time (10^{-4} s to 10^4 s). Determination of the Prony series parameters was then carried out by employing the collocation method proposed by Park and Schapery [66]. By adopting the three-step approach (i.e., first with the three-parameter generalized power law, generate time-dependent relaxation modulus data, and then using the Prony series for the generalized Maxwell model), the computational cost incurred during the iterative process could be significantly reduced and the efficiency of the DIC-FEM inverse process was increased.

Figure 13(a) shows the convergence of the objective function, which was calculated from a total of 35 nodes (locations). As the figure presents, the inverse method rapidly converged at around 20 iterations, and the function saturated fully at about 100 iterations. Figure 13(b) presents the resulting displacements when using the optimized linear viscoelastic property (i.e., time-dependent relaxation modulus).

low noise cameras, high-resolution speckle patterns, and improved DIC algorithm that minimize noise [47]. Furthermore, as indicated earlier, the three-point beam testing that does not consider three-dimensional deformation in particular with the anticlastic curvature is not feasible to effectively characterize Poisson' ratio.

In this study, both the DIC measurements and FEM model simulations (plane stress condition) were conducted in two-dimensional space. Therefore, Poisson's ratio was assumed reasonably with a constant of 0.35 [60, 64], and the relaxation modulus $E(t)$ was sought through the DIC-FEM inverse optimization process.

The main complexity of determining linear viscoelastic properties using the DIC-FEM inverse method arises from the many Prony series terms required to represent a certain relaxation function. To address this, the relaxation function was initially postulated to be a generalized power law [62] that involved three model parameters (i.e.,,E_p, E_q, and r) for the DIC-FEM optimization. The generalized power law is shown below.

Fig. 14 Comparison of deflection results from the FEM, the experiment (i.e., DIC), and analytical solution calculated using results from the DIC-FEM inverse method
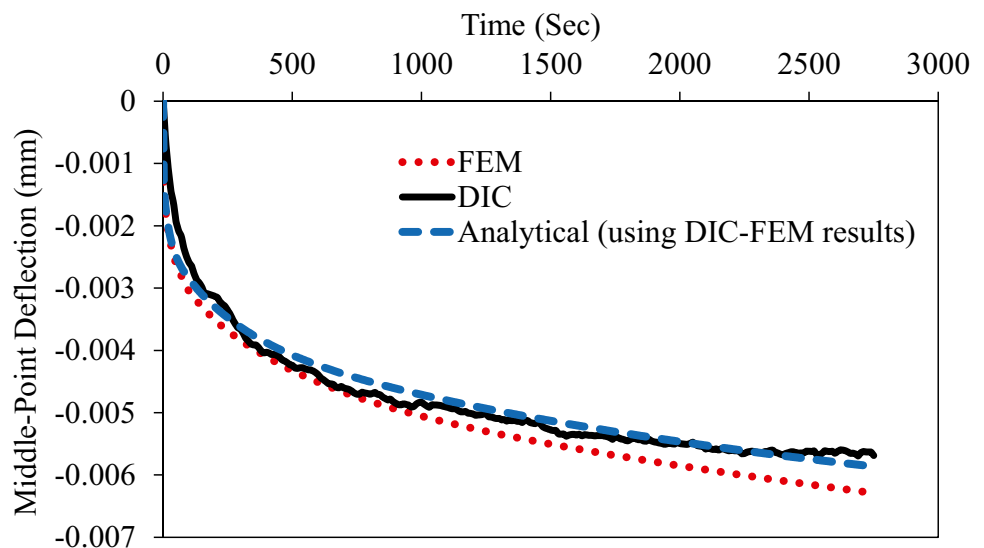
Five different locations were arbitrarily selected to demonstrate the agreement between DIC experimental results and FEM computational simulations. The results in Fig. 13(b) show a varying level of agreement in the vertical displacements resulting from the DIC measurements and the FEM model simulations. Generally, the time-dependent displacements were in good agreement, which implies the validity of the DIC-FEM inverse process in identifying unknown linear viscoelastic material properties, such as relaxation modulus.

Based on the results from the DIC-FEM inverse method in Fig. 13, the analytical solution to the displacement at the center of the FAM beam specimen was calculated using Eq. (8). The resulting Prony series parameters of the generalized Maxwell model are shown in Table 1. Figure 14 shows the results from the analytical solution compared to the FEM and DIC test results. Both the analytically obtained deflections and the FEM deflections that used the linear viscoelastic relaxation modulus identified through the inverse method were in good agreement with experimental DIC results. The good agreement between the deflection results implies that the DIC-FEM inverse method implemented in this study is valid for the characterization of linear viscoelastic properties of materials.

Summary and Conclusions

This study pursued incorporating local field displacements into the identification of constitutive properties of linear elastic and linear viscoelastic materials. Local deformation from experimental testing using DIC was integrated with FEM results to form an inverse problem. This was then solved using a nonlinear optimization framework implemented in Python, MATLAB, and Batch. The DIC-FEM inverse framework solely utilized field displacements inside a region of interest to identify the constitutive properties of two example materials: PEEK (elastic) and a bituminous FAM (viscoelastic). Based on the results, the following can be concluded:

- DIC proved that field deformation can be effectively captured and meaningfully used to determine material properties. Local field displacements were successfully used to characterize properties of both linear elastic and linear viscoelastic materials after being coupled with computational FEM simulations and a nonlinear optimization algorithm.

- The DIC-FEM inverse method successfully identified Young's modulus of an example linear elastic PEEK and the linear viscoelastic relaxation modulus of the FAM. The constitutive properties that resulted from the DIC-FEM nonlinear optimization were successfully validated through the analytical solutions and representative values reported in the literature.

- Further studies are recommended to expand the DIC-FEM inverse method to include fracture, heterogeneity, and Poisson effects of materials. Using strains in addition to displacements is also recommended for a more accurate characterization of deformation. The authors are currently working on these expansions, and the results will be presented in follow-up studies.

Declarations

Competing Interests The authors have no competing interests to declare that are relevant to the content of this article.

Conflicts of Interests The authors have no conflicting interests to declare that are relevant to the content of this article.

References

1. Zhao J, Dong J, Liu Z, Xie H (2019) Characterization method of mechanical properties of rubber materials based on in-situ stereo finite-element-model updating. Polym Testing 79:106015
2. Chu T, Ranson W, Sutton MA (1985) Applications of digital-image-correlation techniques to experimental mechanics. Exp Mech 25(3):232–244. https://doi.org/10.1007/BF02325092
3. McCormick N, Lord J (2010) Digital image correlation. Mater Today 13(12):52–54. https://doi.org/10.1016/S1369-7021(10)70235-2
4. Bruck H, McNeill S, Sutton MA, Peters W (1989) Digital image correlation using Newton-Raphson method of partial differential correction. Exp Mech 29(3):261–267
5. Yoneyama S (2016) Basic principle of digital image correlation for in-plane displacement and strain measurement. Adv Compos Mater 25(2):105–123. https://doi.org/10.1080/09243046.2015.1129681
6. Shen B, Paulino G (2011) Direct extraction of cohesive fracture properties from digital image correlation: a hybrid inverse technique. Exp Mech 51(2):143–163
7. Shao X, Dai X, He X (2015) Noise robustness and parallel computation of the inverse compositional Gauss-Newton algorithm in digital image correlation. Opt Lasers Eng 71:9–19. https://doi.org/10.1016/j.optlaseng.2015.03.005
8. Gajewski T, Garbowski T (2014) Calibration of concrete parameters based on digital image correlation and inverse analysis. Archives of Civil and Mechanical Engineering 14(1):170–180. https://doi.org/10.1016/j.acme.2013.05.012
9. Genovese K, Casaletto L, Humphrey JD, Lu J (2014) Digital image correlation-based point-wise inverse characterization of heterogeneous material properties of gallbladder in vitro. Proceedings of the Royal Society A: Mathematical, Physical and Engineering Sciences 470(2167):20140152
10. Sutton M, Wolters W, Peters W, Ranson W, McNeill S (1983) Determination of displacements using an improved digital correlation method. Image Vis Comput 1(3):133–139
11. Sutton M, Mingqi C, Peters W, Chao Y, McNeill S (1986) Application of an optimized digital correlation method to planar deformation analysis. Image Vis Comput 4(3):143–150

12. Jiang Y, Li G-Y, Qian L-X, Hu X-D, Liu D, Liang S, Cao Y (2015) Characterization of the nonlinear elastic properties of soft tissues using the supersonic shear imaging (SSI) technique: inverse method, ex vivo and in vivo experiments. Med Image Anal 20(1):97–111

13. He W, Goudeau P, Le Bourhis E, Renault P-O, Dupré JC, Doumalin P, Wang S (2016) Study on Young's modulus of thin films on Kapton by microtensile testing combined with dual DIC system. Surf Coat Technol 308:273–279

14. He W, Han M, Goudeau P, Le Bourhis E, Renault P-O, Wang S, Li L-A (2018) Strain transfer through film-substrate interface and surface curvature evolution during a tensile test. Appl Surf Sci 434:771–780

15. He W, Duan Q, Shi W, Xie H (2019) Elastic property characterization of soft substrate-supported thin films using multiscale digital image correlation. Opt Lasers Eng 121:112–119

16. Tuninetti V, Gilles G, Péron-Lührs V, Habraken A (2012) Compression test for metal characterization using digital image correlation and inverse modeling. Procedia IUTAM 4:206–214

17. Laurin F, Charrier J-S, Lévêque D, Maire J-F, Mavel A, Nuñez P (2012) Determination of the properties of composite materials thanks to digital image correlation measurements. Procedia IUTAM 4:106–115

18. Caminero MA, Lopez-Pedrosa M, Pinna C, Soutis C (2013) Damage monitoring and analysis of composite laminates with an open hole and adhesively bonded repairs using digital image correlation. Compos B Eng 53:76–91

19. Ghiassi B, Xavier J, Oliveira DV, Lourenço PB (2013) Application of digital image correlation in investigating the bond between FRP and masonry. Compos Struct 106:340–349

20. Kubo S (1988) Inverse problems related to the mechanics and fracture of solids and structures. JSME international journal. Ser. 1. Solid Mechanics, Strength Mater 31(2):157–166

21. Lin L, Li H, Fok AS, Joyce M, Marrow J (2008) Characterization of heterogeneity and nonlinearity in material properties of nuclear graphite using an inverse method. J Nucl Mater 381(1–2):158–164. https://doi.org/10.1016/j.jnucmat.2008.07.042

22. Lin L, Li H, Fok AS, Joyce M, Marrow TJ (2006) Characterization of material properties using an inverse method. Vol. 5. Trans Tech Publ

23. Nguyen T, Boyce B (2011) An inverse finite element method for determining the anisotropic properties of the cornea. Biomech Model Mechanobiol 10(3):323–337. https://doi.org/10.1007/s10237-010-0237-3

24. Kim SK, Jung BS, Kim HJ, Lee WI (2003) Inverse estimation of thermophysical properties for anisotropic composite. Exp Thermal Fluid Sci 27(6):697–704. https://doi.org/10.1016/S0894-1777(02)00309-6

25. Schnur DS, Zabaras N (1992) An inverse method for determining elastic material properties and a material interface. Int J Numer Meth Eng 33(10):2039–2057. https://doi.org/10.1002/nme.1620331004

26. Mathieu F, Leclerc H, Hild F, Roux S (2015) Estimation of elastoplastic parameters via weighted FEMU and integrated-DIC. Exp Mech 55(1):105–119

27. Pan B (2018) Digital image correlation for surface deformation measurement: historical developments, recent advances and future goals. Meas Sci Technol 29(8):082001

28. Grédiac M (1989) Principe des travaux virtuels et identification. Comptes rendus de l'Académie des sciences. Série 2, Mécanique, Physique, Chimie. Sciences de l'univers, Sciences de la Terre 309(1):1–5

29. Pierron F, Grédiac M (2012) The virtual fields method: extracting constitutive mechanical parameters from full-field deformation measurements. Springer Science & Business Media

30. Pierron F, Forquin P (2012) Ultra-high-speed full-field deformation measurements on concrete spalling specimens and stiffness identification with the virtual fields method. Strain 48(5):388–405

31. Brigham J, Aquino W, Mitri F, Greenleaf JF, Fatemi M (2007) Inverse estimation of viscoelastic material properties for solids immersed in fluids using vibroacoustic techniques. J Appl Phys 101(2):023509. https://doi.org/10.1063/1.2423227

32. Lutif JE, Souza FV, Kim YR, Soares JB and Allen DH (2010) Multiscale modeling to predict mechanical behavior of asphalt mixtures. Trans Res Rec 2181(1):28–35. https://doi.org/10.3141/2181-04

33. Shen B, Stanciulescu I, Paulino GH (2010) Inverse computation of cohesive fracture properties from displacement fields. Inverse Probl Sci Eng 18(8):1103–1128

34. Shen B, Paulino GH (2011) Identification of cohesive zone model and elastic parameters of fiber-reinforced cementitious composites using digital image correlation and a hybrid inverse technique. Cement Concr Compos 33(5):572–585

35. Shen B, Functionally graded fiber-reinforced cementitious composites—Manufacturing and extraction of cohesive fracture properties using finite elements and digital image correlation. Civil Engineering. Vol. Doctor of Philosophy. (2009) Urbana. University of Illinois at Urbana-Champaign, Illinois

36. Geymonat G, Hild F, Pagano S (2002) Identification of elastic parameters by displacement field measurement. CR Mec 330(6):403–408. https://doi.org/10.1016/S1631-0721(02)01476-6

37. Kiełczyński P, Szalewski M (2011) An inverse method for determining the elastic properties of thin layers using Love surface waves. Inverse Problems in Science and Engineering 19(1):31–43. https://doi.org/10.1080/17415977.2010.531472

38. Ruggiero L, Sol H, Sahli H, Adriaenssens S, Adriaenssens N (2011) An inverse method to determine material properties of soft tissues. Mechanics of Biological Systems and Materials 2:19–32. https://doi.org/10.1007/978-1-4614-0219-0_3

39. Lin L (2009) Characterization of Material Properties Using Inverse Method Ann Arbor: The University of Manchester (United Kingdom). 209. https://scholar.uwindsor.ca/etd/4825

40. Mathieu F, Leclerc H, Hild F and Roux S (2015) Estimation of elastoplastic parameters via weighted FEMU and integrated-DIC. Experimen Mech 55:105–119

41. de-Carvalho R, Valente RAF, Andrade-Campos A (2011) Optimization strategies for non-linear material parameters identification in metal forming problems. Comp and Struct 89:246–255

42. Gajewski M, Kowalewski L (2016) Inverse analysis and DIC as tools to determine material parameters in isotropic metal plasticity with isotropic strain hardening. Mater Test 58(10). https://doi.org/10.3139/120.110925

43. Im S, Kim Y-R, Ban H (2013) Rate-and Temperature-Dependent Fracture Characteristics of Asphaltic Paving Mixtures. J Test Eval 41(2):257–268

44. Kim YR, Teixeira JE, Kommidi SR, Little DN, Aragao FT, Manrique-Sanchez L, Souza FV (2021) Rate-dependent fracture modeling of bituminous media using nonlinear viscoelastic cohesive zone with Gaussian damage function. Comput -Aided Civ Infrastruct Eng

45. Abaqus V (2014) 6.14 Documentation, in Dassault Systemes Simulia Corporation 6.2

46. Kowalewski Ł, Gajewski M (2019) Assessment of Optimization Methods Used to Determine Plasticity Parameters Based on DIC and back Calculation Methods. Exp Tech 43(4):385–396

47. Sutton MA, Orteu JJ, Schreier H (2009) Image correlation for shape, motion and deformation measurements: basic concepts, theory and applications. Springer Science & Business Media

48. Negahban M (2012) The mechanical and thermodynamical theory of plasticity. Crc New York, NY

49. Vendroux G, Knauss W (1998) Submicron deformation field measurements: Part 2. Improved digital image correlation Experimental Mechanics 38(2):86–92

50. Lu H, Cary P (2000) Deformation measurements by digital image correlation: implementation of a second-order displacement gradient. Exp Mech 40(4):393–400

51. Lagarias JC, Reeds JA, Wright MH, Wright PE (1998) Convergence properties of the Nelder-Mead simplex method in low dimensions. SIAM J Optim 9(1):112–147

52. Singer S, Nelder J (2009) Nelder-mead algorithm Scholarpedia 4(7):2928. https://doi.org/10.4249/scholarpedia.2928

53. Barton RR, Ivey JS Jr (1991). Modifications of the Nelder-Mead simplex method for stochastic simulation response optimization. https://doi.org/10.1109/WSC.1991.185709

54. Nocedal J and Wright S (2006) Numerical optimization. Springer Science & Business Media

55. Anderson TL (2017) Fracture mechanics: fundamentals and applications. CRC press

56. El-Qoubaa Z, Othman R (2015) Characterization and modeling of the strain rate sensitivity of polyetheretherketone's compressive yield stress. Mater and Des (1980–2015) 66:336–345

57. Rivard CH, Rhalmi S, Coillard C (2002) In vivo biocompatibility testing of peek polymer for a spinal implant system: a study in rabbits. Journal of Biomedical Materials Research: An Official Journal of The Society for Biomaterials, The Japanese Society for Biomaterials, and The Australian Society for Biomaterials and the Korean Society for Biomaterials 62(4):488–498

58. Chen F, Ou H, Lu B, Long H (2016) A constitutive model of polyether-ether-ketone (PEEK). J Mech Behav Biomed Mater 53:427–433

59. Chen F, Gatea S, Ou H, Lu B, Long H (2016) Fracture characteristics of PEEK at various stress triaxialities. J Mech Behav Biomed Mater 64:173–186

60. Aragão FTS, Kim YR (2012) Mode I Fracture Characterization of Bituminous Paving Mixtures at Intermediate Service Temperatures. Exp Mech 52(9):1423–1434. https://doi.org/10.1007/s11340-012-9594-4

61. Al-Rub RKA, Darabi MK, You T, Masad EA, Little DN (2011) A unified continuum damage mechanics model for predicting the mechanical response of asphalt mixtures and pavements. Int J Roads Airports 1(1):68–84

62. Im S, You T, Ban H, Kim Y-R (2017) Multiscale testing-analysis of asphaltic materials considering viscoelastic and viscoplastic deformation. Int J Pavement Eng 18(9):783–797

63. Aragão FTS, Badilla-Vargas GA, Hartmann DA, de Oliveira AD, Kim Y-R (2017) Characterization of temperature-and rate-dependent fracture properties of fine aggregate bituminous mixtures using an integrated numerical-experimental approach. Eng Fract Mech 180:195–212

64. Kim Y-R, Aragao FT, Allen DH, Little DN (2010) Damage modeling of bituminous mixtures considering mixture microstructure, viscoelasticity, and cohesive zone fracture. Can J Civ Eng 37(8):1125–1136

65. Ban H, Im S, Kim Y-R (2015) Mixed-mode fracture characterization of fine aggregate mixtures using semicircular bend fracture test and extended finite element modeling. Constr Build Mater 101:721–729

66. Park S and Schapery R (1999) Methods of interconversion between linear viscoelastic material functions. Part I—A numerical method based on Prony series. Int J Solid Struct 36(11):1653–1675

67. Newcomb D, Martin AE, Yin F, Arambula E, Park ES, Chowdhury A, Brown R, Rodezno C, Tran N, Coleri E (2015) Short-term laboratory conditioning of asphalt mixtures

68. Wineman AS and Rajagopal KR (2000) Mechanical response of polymers: an introduction. Cambridge University Press

69. Haque A (2019) Timoshenko Beam Theory. Independently published

70. Gutierrez-Lemini D (2014) Engineering viscoelasticity. Springer

71. Cowper G (1966) The shear coefficient in Timoshenko's beam theory

72. Sobieraj MC, Kurtz SM, Rimnac CM (2009) Notch sensitivity of PEEK in monotonic tension. Biomaterials 30(33):6485–6494

73. Kurtz SM (2019) PEEK biomaterials handbook. William Andrew

74. Jaekel DJ, MacDonald DW, Kurtz SM (2011) Characterization of PEEK biomaterials using the small punch test. J Mech Behav Biomed Mater 4(7):1275–1282

75. Lesiuk G, Sawicka A, Correia J, Frątczak R (2017) Fracture resistance analysis of PEEK-polymer. Engineering Structures and Technologies 9(4):207–213

76. Tschoegl NW, Knauss WG, Emri I (2002) Poisson's ratio in linear viscoelasticity–a critical review. Mechanics of Time-Dependent Materials 6(1):3–51

77. Lu H, Zhang X, Knauss W (1997) Uniaxial, shear, and Poisson relaxation and their conversion to bulk relaxation: studies on poly (methyl methacrylate). Polym Compos 18(2):211–222